High-speed nanoscopic tracking of the position and orientation of a single virus

Philipp Kukura[1], Helge Ewers[1,2], Christian Müller[1,3], Alois Renn[1], Ari Helenius[2] & Vahid Sandoghdar[1]

Optical studies have revealed that, after binding, virions move laterally on the plasma membrane, but the complexity of the cellular environment and the drawbacks of fluorescence microscopy have prevented access to the molecular dynamics of early virus-host couplings, which are important for cell infection. Here we present a colocalization methodology that combines scattering interferometry and single-molecule fluorescence microscopy to visualize both position and orientation of single quantum dot–labeled Simian virus 40 (SV40) particles. By achieving nanometer spatial and 8 ms temporal resolution, we observed sliding and tumbling motions during rapid lateral diffusion on supported lipid bilayers, and repeated back and forth rocking between nanoscopic regions separated by 9 nm. Our findings suggest recurrent swap of receptors and viral pentamers as well as receptor aggregation in nanodomains. We discuss the prospects of our technique for studying virus-membrane interactions and for resolving nanoscopic dynamics of individual biological nano-objects.

In the past two decades, several ingenious experiments have demonstrated that fluorescence microscopy can be used to access spatial information beyond the diffraction limit and down to the nanometer level[1–7]. One of the key technologies for this revival of optical microscopy is the sensitive detection of a single fluorescent molecule or nano-object[8,9] and consequently the possibility to localize it spatially. In localization, the center of mass of a nano-object is deduced by analyzing and fitting its point spread function. The signal-to-noise ratio (SNR) of the measurement determines the accuracy in finding the position of the nano-object[10]. Despite its many successes in biological applications[11,12], fluorescence-based localization is confronted with fundamental barriers. Photobleaching restricts the observation time to the order of a minute, and fluorescence saturation limits the detected photon flux and, thus, the localization accuracy and imaging speed. Furthermore, conventional center-of-mass localization cannot provide access to the internal orientational dynamics of the object.

To circumvent these shortcomings, we have developed an interferometric scattering (iSCAT) detection method[13,14], in which a laser beam is focused tightly on the sample, and the incident light partially reflected at the substrate-water interface is collected together with the light scattered by the nano-object of interest (**Fig. 1a**). The detector measures the intensity of the total light field $E_{tot} = E_{ref} + E_{sca}$, in which E_{ref} and E_{sca} denote the electric fields of the reflected and scattered components, respectively. For weak E_{sca}, the resulting interference signal $I_{int} \propto E_{ref}\, E_{sca}$ dominates the pure scattering signal given by $I_{sca} \propto |E_{sca}|^2$. The imaging contrast of interest becomes then $S \cong I_{int} / I_{ref}$, in which I_{ref} is the intensity of the reflected light[13]. For shot noise–limited detection, the SNR in iSCAT can be approximated by $S \times N^{1/2}$, in which N is the number of detected photons. Thus, the localization accuracy in this method can be largely improved by increasing the incident light power. Furthermore, large iSCAT signals generated by high illumination powers allow short integration times and therefore exquisite time resolution[14]. Lastly, iSCAT provides a label-free detection method[15] that is of enormous advantage for biological studies.

In this work, we monitored the center of mass of single virus-like particles (VLPs) by iSCAT and simultaneously traced a fluorescent quantum dot (QD) attached to the VLP surface. In this fashion, we not only imaged the position of the virion but also determined its orientation in real time. The virus we chose was Simian virus 40 (SV40), a non-enveloped DNA virus with a diameter of 45 nm. The outer shell is composed of 72 pentamers of viral protein 1 (VP1) organized with $T = 7$ icosahedral symmetry[16] (**Fig. 1b**). Each VP1 molecule has a binding site for the glycan moiety of GM1 ganglioside[17,18] present in the outer leaflet of the host cell plasma membrane. By binding to several GM1 molecules, SV40 is thought to induce its own lipid-dependent confinement and endocytosis after a period of lateral diffusion in the plane of the membrane (data not shown). However, several fundamental questions about the nanoscale organization and dynamics of the virus-receptor complex remain open. Does the virus slide on the membrane with a fixed cohort of receptors, or does it exchange receptors in a dynamic fashion? How do rotational and translational diffusion compare? How is viral motion affected by receptor concentration and the resulting membrane structure? Here we address several of these questions by directly visualizing the nanoscale motion of single virions that diffuse on supported lipid bilayers. In particular, we observed a sliding

[1]Laboratory of Physical Chemistry and [2]Institute of Biochemistry, Eidgenössische Technische Hochschule (ETH) Zurich, Zurich, Switzerland. [3]Present address: Laboratory of Organic Chemistry, ETH Zurich, Zurich, Switzerland. Correspondence should be addressed to V.S. (vahid.sandoghdar@ethz.ch).

RECEIVED 28 APRIL; ACCEPTED 24 SEPTEMBER; PUBLISHED ONLINE 1 NOVEMBER 2009; DOI:10.1038/NMETH.1395

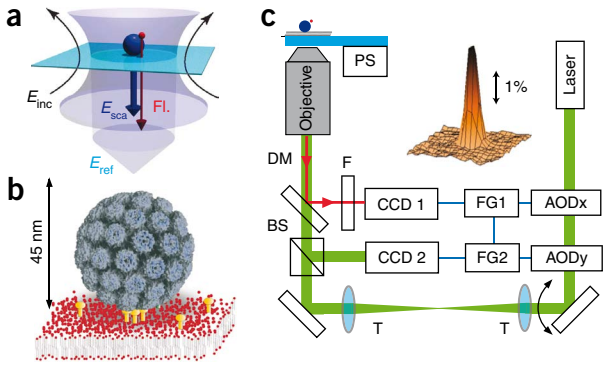

Figure 1 | iSCAT experimental approach. (**a**) A QD-labeled VLP is illuminated in the focus of a laser beam. The light scattered by the VLP and the QD fluorescence are detected simultaneously. E_{inc}, incident light field; E_{sca}, scattered light field; E_{ref}, reflected light field; Fl., QD fluorescence emission. (**b**) Sample arrangement including SV40, a supported lipid bilayer and incorporated GM1 molecules (yellow). (**c**) Schematic of the experimental setup. PS, piezo scanner; objective, oil immersion microscope objective with numerical aperture of 1.4; DM, dichroic mirror; BS, 50:50 beam splitter; F, long-pass filter; T, telecentric lens imaging system; FG, function generator; AODx and AODy, acousto-optic deflectors for the *x* and *y* directions in the sample plane. Inset, surface plot representing a typical iSCAT point spread function for a single SV40 VLP. The surface plot is inverted for clarity.

motion consistent with virus binding to multiple receptors in the membrane, a tumbling motion that indicates rapid exchange of binding pentamers and bound receptors and a nanoscopic rocking motion that suggests digital exchange of binding pentamers when bound to immobile receptor aggregates in the supported lipid bilayers.

RESULTS

High-speed nanometric tracking of viral position and orientation

Although the interferometric character of iSCAT amplifies the scattering signal compared to a direct measurement of the scattering intensity, one has to consider several limitations. Signals from tiny particles are generally small and have to be detected on top of a large laser intensity background. Thus, any laser power fluctuations or detector noise reduce the SNR and eventually mask small signals completely. Additionally, background scattering caused by surrounding objects or substrate roughness makes it difficult to identify the signal of interest and reduce the effective SNR. Here we present an approach that avoids these difficulties and enables fast and shot noise–limited iSCAT imaging of biological nano-objects.

In our experimental setup (**Fig. 1c**), the output of a low-noise solid-state laser at 532 nm was rapidly scanned across the sample using two acousto-optic deflectors. Scattered and reflected light collected by a microscope objective (numerical aperture, 1.4) was split by a 50:50 beam splitter and imaged onto a charge-coupled device (CCD). CCDs enable fast image capture as well as shot noise–limited detection of the incident light because camera noise is lower than shot noise–induced intensity fluctuations. The high deflection speed of acousto-optic deflectors generated an evenly illuminated region on the time scale of a single CCD exposure. By adjusting the laser intensity and imaging configuration (Online Methods) we detected about 10^6 photoelectrons for an imaged area of (100 × 100 nm) in each exposure, resulting in shot noise–limited background fluctuations on the order of 10^{-3} and a high SNR obtained for an iSCAT signal of 3% from a single SV40 VLP (**Fig. 1c**). To eliminate the residual scattering signals caused by membrane impurities, substrate roughness and spurious reflections in the optical setup, we used an image subtraction scheme (**Supplementary Fig. 1**). To image the attached QD simultaneously with the iSCAT signal of the VLP, we placed a dichroic mirror and a second CCD in the beam path and overlapped iSCAT and fluorescence images with 3 nm accuracy using a published procedure[19] (**Supplementary Fig. 2**). We synchronized image acquisition and beam scanning with <50 µs accuracy using function generators.

We used biotinylated VLPs that consist of the empty protein capsid of SV40, without its DNA genome, bound to a dioleoylphosphatidylcholine (DOPC)-based supported lipid bilayer doped with the cellular receptor GM1. Addition of streptavidin-functionalized fluorescent QDs resulted in VLPs labeled with single QDs. In iSCAT images of individual membrane-bound VLPs, virions appeared as dark spots (**Fig. 2a**). A simultaneously acquired fluorescence image of the QD labels (**Fig. 2b**), indicated that in this case two out of the three VLPs have been labeled. We never observed binding of multiple QDs to a single virion, as checked by fluorescence blinking. Analysis of the localization accuracies for the virion center of mass (VCM) determined for 400 consecutive iSCAT images revealed an average two-dimensional precision of 2.2 nm (**Fig. 2c**). The observed narrow and symmetric distribution originated from the intensity stability (**Fig. 2c**) and high SNR of iSCAT signals (**Supplementary Video 1**). We estimate the iSCAT signal of a QD to be ~0.1% in our configuration based on previous results on iSCAT detection of the same QDs[20]. Given the virus signal of 3%, the shot noise–limited background fluctuations of

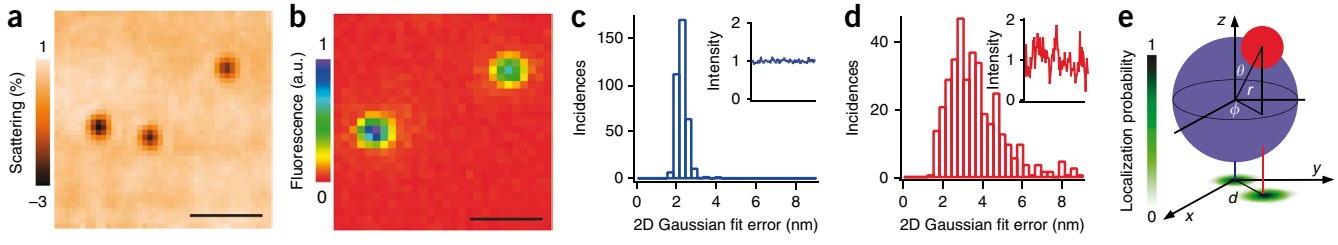

Figure 2 | Determination of localization accuracy and orientation. (**a**,**b**) Representative interferometric scattering image of individual SV40 VLPs (**a**) and a corresponding simultaneously acquired fluorescence image (**b**). Scale bars, 1 µm. (**c**,**d**) Histogram of localization accuracies obtained from Gaussian fitting for 400 consecutive scattering images of a single virus (**c**) and equivalent plot for QD fluorescence attached to the same virus (**d**). Insets, normalized signal amplitude for iSCAT and fluorescence signals obtained from 100 consecutive frames. (**e**) Determination of the distance, *d*, the polar angle, *θ*, and the azimuthal angle, *ϕ*, of a VLP (blue) bound by a QD (red) from the scattering and fluorescence centers of mass obtained by localization (green).

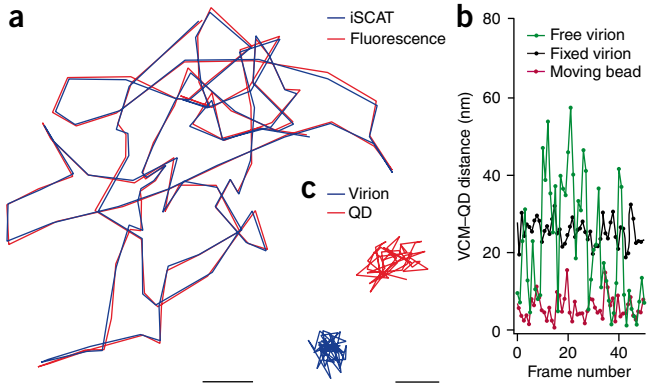

Figure 3 | iSCAT control experiments. (**a**) Scattering and fluorescence trajectories created from 100 consecutive images of a piezo-translated fluorescent bead imaged at the same speed and localization accuracy as for a diffusing virus. Scale bar, 100 nm. (**b**) Distance between iSCAT and fluorescence signals from 50 consecutive images of a moving bead, a fixed virion-QD construct and a diffusing virion-QD construct (trajectories in **Fig. 4a**). (**c**) Simultaneous iSCAT and QD fluorescence traces for a labeled virion that was fixed on a glass substrate from 50 consecutive images. Scale bar, 10 nm.

0.1% and the short virus-QD distance, we verified theoretically that QD scattering can be neglected in the determination of the VCM. The limited photophysics of the QD, in contrast, result in a broader and asymmetric localization histogram with an average accuracy of 3.7 nm for the same 400 images (**Fig. 4d**). Assuming a rigid link between the virion and the QD, the knowledge of x_{VCM}, y_{VCM} and x_{QD}, y_{QD} allowed us to deduce the distance d and angle ϕ uniquely (**Fig. 2e**). Moreover, we know $r \cong 36$ nm, determined from the virion diameter of 45 nm, the linker length of 4 nm and the QD diameter of 15–20 nm. Therefore, we can calculate $\arcsin(d/r)$ corresponding to θ or $\pi - \theta$. This ambiguity, however, had no consequences for the conclusions drawn in this work as they rely solely on the observation of correlated internal rotation and center-of-mass translation rather than the full three-dimensional elucidation of viral motion.

To determine whether the observed dynamics were representative of viral motion, we used a piezoelectric scanner to randomly move a polymer bead (diameter of 100 nm), that had been homogeneously doped with fluorescent dyes, at a speed comparable to that of a diffusing virion. By adjusting the incident light intensity, we reached accuracies in both fluorescence and iSCAT channels comparable to those in the virus experiment. The centers of mass of the fluorescence and scattering signals matched very well throughout their trajectories (**Fig. 3a**,**b**). Furthermore, to ensure that r did not vary with time, we monitored single labeled virions that we directly attached to cover glass and thus fixed in space. The resulting virus and QD trajectories (**Fig. 3c**) and the corresponding distance d (**Fig. 3b**) remained constant throughout the measurement, indicating that deformation of the virus, flexibility of the virus-QD linkage and motion of the QD on the surface of the virion were negligible within the experimental error. These results were in stark contrast to the behavior of a supported lipid bilayer–bound mobile virion discussed below (**Figs. 3b** and **4a**).

SV40 motion at low receptor concentration

Having achieved nanometer resolution in colocalization of the iSCAT and fluorescence channels, we generated trajectories by acquiring images every 8 ms and connecting the virion and QD positions determined by localization in each frame. The resulting trajectories trace the overall random-seeming motion of a single virion at 0.05% receptor concentration (**Fig. 4a**). However, the two trajectories did not overlap.

The short exemplary segment shown in **Figure 4b** demonstrates that QD and VCM maintained their separation during a journey of several hundred nanometers. This is consistent with a sliding motion of the virion along the membrane with possible changes in the azimuthal angle, ϕ, but without any substantial rotation about the polar angle, θ. In contrast, we observed a segment in which d fluctuated repeatedly (**Fig. 4c**), indicating a change in θ. To help visualize the tumbling motion of the virion, we reconstructed the full three-dimensional motion of the virion and QD from this segment (**Fig. 4d**). During the first 14 ms, the virion appeared to diffuse without a substantial modification of its contact point with the membrane. In the subsequent images, however, we observed a considerable change in θ and a clear shift in the location of the virion-membrane junction and thus an exchange of receptors and binding pentamers. A representative movie of 200 such consecutive images is available (**Supplementary Video 2**).

Parallel QD and VCM trajectories (**Fig. 4a**,**b**) indicate that virions rotated in the plane of the membrane on the time scale of

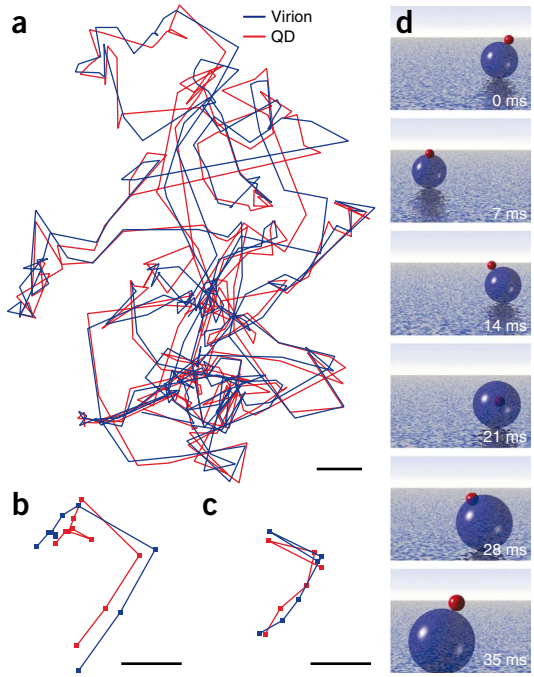

Figure 4 | Diffusion at low (0.05 mol%) GM1 concentration. (**a**) Virion and QD trajectories from 300 consecutive iSCAT imaging frames acquired with an exposure time of 7.5 ms per image (130 frames s^{-1}). (**b**,**c**) Close-ups of two short (<10 frames) fragments from the trajectories in **a** exhibiting sliding and tumbling motion. Scale bars, 100 nm. (**d**) Three-dimensional rendering of the motion of the virion carrying the QD on a supported lipid bilayer. The data were extracted from the trajectories in **c**, sequentially from top to bottom.

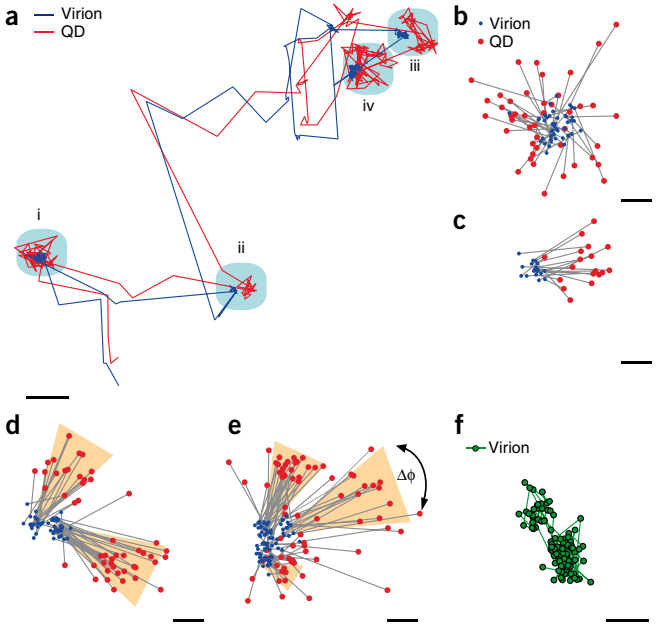

Figure 5 | Diffusion at high (1 mol%) GM1 concentration. (**a**) Virion and QD trajectories from 250 consecutive iSCAT imaging frames acquired with an exposure time of 20 ms per image (25 frames s^{-1}). Scale bar, 50 nm. (**b**–**e**) Zoom of the highlighted sections i–iv in **a**. The blue and red dots represent the positions of the virion and the QD, respectively. The gray lines connect the corresponding positions in each exposure. The orange triangles highlight the confinement of ϕ. (**f**) iSCAT map of a rocking motion for an unlabeled virion. Scale bars, 10 nm.

hundreds of milliseconds. Based on these observations, it is likely that the virion must be bound by several receptors even at a low receptor concentration of about 0.05%, given a predicted rotational diffusion time for the virus-receptor complex in aqueous medium on the order of 50 μs according to the Stokes-Einstein-Debye formula[21]. This notion is supported by the observation that SV40 VLPs exhibit diffusion coefficients below 0.1 $\mu m^2 s^{-1}$ (ref. 15) compared to 2 $\mu m^2 s^{-1}$ for fluorophore-labeled GM1 as measured by fluorescence recovery after photobleaching (FRAP).

SV40 motion at high receptor concentration

To explore the effect of receptor concentration on virus motion, we increased the GM1 content 20-fold to 1 mol%, corresponding to an average of about 2 GM1 lipids within an area of (10 × 10 nm). At this concentration, the lipid bilayer is still fluid and GM1 highly mobile with a diffusion coefficient of = 1.9 ± 0.3 $\mu m^2 s^{-1}$ as confirmed by FRAP experiments of a headgroup-labeled GM1 isoform. When we added SV40 VLPs to such bilayers, we observed a drastic difference in the diffusive behavior of the virion with most virions remaining stationary even over several minutes (data not shown). In some cases, periods of standstill were followed by rapid diffusion (**Fig. 5a**), bearing a striking similarity with single SV40 trajectories observed on living cells[22]. The high localization resolution in our experiment revealed, however, that the virions were not fully immobile during the standstill periods (**Fig. 5b–e**). In one case, the QD covered a wide range of ϕ and θ, and the VCM explored a region of about 20 nm (**Fig. 5b**). In contrast, the VCM could be confined to a nanodomain smaller than 10 nm for almost 1 s (**Fig. 5c**). Moreover, the iSCAT signals exhibited digital stepping motion of the virion between two or more distinct nanodomains spaced by 8.5 ± 2.5 nm (**Fig. 5d**,**e**). In each case, VCM stepping was clearly correlated with the confinement of the QD and quantization of the angle ϕ within a spread $\Delta\phi$, well beyond the measurement uncertainty. In fact, the virion rocked back and forth between these well-defined nanodomains many times (**Supplementary Videos 3–6**). To ensure that the observed effects were not caused by the presence of the QD, we performed the same experiment virions that had no QDs attached (**Fig. 5f**) and found that the VCM rocking still occurred (**Supplementary Video 7**).

DISCUSSION

During our measurements, we examined the behavior of about 100 virions and analyzed the trajectories of a dozen in detail. We showed selected trajectories that displayed various phenomena that we encountered among individual trajectories. In this work, we refrained from quantification of effects such as rocking, sliding and tumbling. A full statistical analysis of each occurrence and its dependence on various membrane and receptor parameters requires extensive measurements, and we left this for future studies. Nevertheless, our findings shed light on many central features of the interaction between virions and their receptors.

The virion likely cannot bind with more than a single pentamer because of the limited flexibility of a supported bilayer membrane. However, while the virion is anchored via one pentamer, binding fluctuations to a neighboring pentamer can modulate the orientation of the virus within $\Delta\phi$ and eventually cause it to roll over by several nanometers to the next contact pentamer. Indeed, the observed VCM step size of 8.5 nm is in agreement with the pentamer spacing of 9 nm in the capsid structure[16], suggesting that the virion rocking was caused by such an exchange of contact pentamers. Moreover, the fact that the virion returned to the same location several times points to the existence of immobile nanoscopic receptor aggregates in the membrane. This hypothesis is consistent with a recent report on the formation of small aggregate domains (<20 nm) of GM1 in structurally similar palmitoyloleoylphosphatidylcholine (POPC) membranes[23] and with the presence of ordered domains at 5 mol% GM1 concentration in dipalmitoylphosphatidylcholine (DPPC) monolayers observed in X-ray studies[24]. Notably, GM1 molecules have also been shown to cluster in cellular membranes[25] and to exhibit nonrandom diffusion[26]. We cannot completely rule out that GM1 clusters are created by membrane defects or transbilayer interaction with the substrate, but the dramatic difference in the trajectories observed with the 0.05 and 1 mol% GM1 concentration suggests that these effects have not been dominant. An intriguing question that arises in the context of virus-receptor interaction is whether the virion induces receptor aggregation or existing aggregates cause immobilization of the virion.

Although observations made on artificial bilayers may not generally apply to physiological conditions, it is likely that the physical mechanisms governing receptor aggregation and virus immobilization reported here also affect virus entry into cells. To gain real-time insight into the mechanical interaction of the virus with a flexible membrane, we are presently working to extend our methodology to imaging on suspended membranes, giant unilamellar vesicles and living cells. As particles of the size and

mobility of virions are abundant in living cells, the key to success in the latter case will be to record and subtract the background scattering (**Supplementary Fig. 1**). By exploiting the nanometer axial localization accuracy of iSCAT, which stems from its intrinsic interferometric nature[27], we hope to visualize the full three-dimensional invagination process, which is only known from static electron microscopy studies[28]. Such dynamic iSCAT studies can then shed light on how lipid-bound cellular ligands induce transmembrane coupling, become immobilized, recruit cellular factors for signaling and cause their internalization. We do not expect iSCAT to track unlabeled nano-objects inside a living cell because of a strong dynamic scattering background. The application of iSCAT to such complex environments might, however, be possible via plasmonic labels[14].

The time resolution and observation time in the work reported here were limited by the photophysics of the QD. However, replacing the fluorescent label with a tiny metallic nanoparticle would avoid these limitations and allow both higher temporal resolution and longer measurements improve this on both extremes of short and long measurement times. A 10 nm gold particle generates the same iSCAT signal as a SV40 VLP and can therefore be localized equally well. To distinguish the iSCAT signals of the virion and the gold label, one can use a second laser and exploit the strong wavelength dependence of the gold particle plasmon resonance[14]. In closing, the spatial and temporal resolutions for imaging of tiny nanoparticles (<50 nm) offered by iSCAT in contrast to previous scattering-based approaches using larger labels[29] can help visualize translation and rotation of biological nano-objects in various systems. In particular, these features pave the way for sophisticated biophysical investigations of fundamental processes such as protein diffusion and nanomotion, which previously have been only accessed by center-of-mass tracking[4,29].

METHODS

Methods and any associated references are available in the online version of the paper at http://www.nature.com/naturemethods/.

Note: Supplementary information is available on the Nature Methods website.

ACKNOWLEDGMENTS

We thank the Swiss Ministry of Education and Research for financial support (EU Integrated project Molecular Imaging), J. Helenius for comments, R. Mancini for providing electron micrographs of quantum dots, A. Oppenheim (Department of Hematology, Hebrew University, Hadassah Medical School and Hadassah Hospital, Jerusalem) for providing SV40 VLPs and Gunter Schwarzmann (Kekule-Institut für Organische Chemie, Universität Bonn) for NBD-GM1. A.H. thanks the Swiss National Science Foundation (SNF) for financial support.

AUTHOR CONTRIBUTIONS

P.K. designed the experimental setup, performed SV40 experiments and analyzed data. H.E. performed FRAP experiments and purified and labeled SV40. H.E. and C.M. prepared supported lipid bilayers. V.S. conceived and supervised the project in collaboration with A.H.; V.S., P.K. and H.E. wrote the manuscript; and P.K., H.E., C.M., A.R., A.H. and V.S. discussed the results and commented on the manuscript.

Published online at http://www.nature.com/naturemethods/.
Reprints and permissions information is available online at http://npg.nature.com/reprintsandpermissions/.

1. Betzig, E. Proposed method for molecular optical imaging. *Opt. Lett.* **20**, 237–239 (1995).
2. Hell, S.W. Far-field optical nanoscopy. *Science* **316**, 1153–1158 (2007).
3. Hettich, C. *et al.* Nanometer resolution and coherent optical dipole coupling of two individual molecules. *Science* **298**, 385–389 (2002).
4. Yildiz, A. *et al.* Myosin V walks hand-over-hand: Single fluorophore imaging with 1.5-nm localization. *Science* **300**, 2061–2065 (2003).
5. Betzig, E. *et al.* Imaging intracellular fluorescent proteins at nanometer resolution. *Science* **313**, 1642–1645 (2006).
6. Rust, M.J., Bates, M. & Zhuang, X. Sub-diffraction-limit imaging by stochastic optical reconstruction microscopy (STORM). *Nat. Methods* **3**, 793–795 (2006).
7. Hess, S.T. *et al.* Dynamic clustered distribution of hemagglutinin resolved at 40 nm in living cell membranes discriminates between raft theories. *Proc. Natl. Acad. Sci. USA* **104**, 17370–17375 (2007).
8. Moerner, W.E. & Orrit, M. Illuminating single molecules in condensed matter. *Science* **283**, 1670–1676 (1999).
9. Weiss, S. Fluorescence spectroscopy of single biomolecules. *Science* **283**, 1676–1683 (1999).
10. Thompson, R.E., Larson, D. & Webb, W. Precise nanometer localization analysis for individual fluorescent probes. *Biophys. J.* **82**, 2775–2783 (2002).
11. Schmidt, T., Schutz, G., Baumgartner, W., Gruber, H. & Schindler, H. Imaging of single molecule diffusion. *Proc. Natl. Acad. Sci. USA* **93**, 2926–2929 (1996).
12. Seisenberger, G. *et al.* Real-time single-molecule imaging of the infection pathway of an adeno-associated virus. *Science* **294**, 1929–1932 (2001).
13. Lindfors, K., Kalkbrenner, T., Stoller, P. & Sandoghdar, V. Detection and spectroscopy of gold nanoparticle using supercontinuum white light confocal microscopy. *Phys. Rev. Lett.* **93**, 037401 (2004).
14. Jacobsen, V., Stoller, P., Brunner, C., Vogel, V. & Sandoghdar, V. Interferometric optical detection and tracking of very small gold nanoparticles at a water-glass interface. *Opt. Express* **14**, 405–414 (2006).
15. Ewers, H. *et al.* Label-free optical detection and tracking of single virions bound to their receptor in supported membrane bilayers. *Nano Lett.* **7**, 2263–2266 (2007).
16. Liddington, R.C. *et al.* Structure of Simian Virus-40 at 3.8-A resolution. *Nature* **354**, 278–284 (1991).
17. Tsai, B. *et al.* Gangliosides are receptors for murine polyoma virus and SV40. *EMBO J.* **22**, 4346–4355 (2003).
18. Neu, U., Woellner, K., Gauglitz, G. & Stehle, T. Structural basis of GM1 ganglioside recognition by Simian Virus 40. *Proc. Natl. Acad. Sci. USA* **105**, 5219–5224 (2008).
19. Churchman, L.S., Okten, Z., Rock, R.S., Dawson, J.F. & Spudich, J.A. Single molecule high-resolution colocalization of Cy3 and Cy5 attached to macromolecules measures intramolecular distances through time. *Proc. Natl. Acad. Sci. USA* **102**, 1419–1423 (2005).
20. Kukura, P., Celebrano, M., Renn, A. & Sandoghdar, V. Imaging a single quantum dot when it is dark. *Nano Lett.* **9**, 926–929 (2009).
21. Einstein, A. A new determination of the molecular dimensions. *Ann. Phys.* **19**, 289–306 (1906).
22. Ewers, H. *et al.* Single-particle tracking of murine polyoma virus-like particles on live cells and artificial membranes. *Proc. Natl. Acad. Sci. USA* **102**, 15110–15115 (2005).
23. Shi, J. *et al.* GM1 clustering inhibits cholera toxin binding in supported phospholipid membranes. *J. Am. Chem. Soc.* **129**, 5954–5961 (2007).
24. Frey, S. *et al.* Condensing and fluidizing effects of ganglioside GM1 on phospholipid films. *Biophys. J.* **94**, 3047–3064 (2008).
25. Fujita, A. *et al.* Gangliosides GM1 and GM3 in the living cell membrane form clusters susceptible to cholesterol depletion and chilling. *Mol. Biol. Cell* **18**, 2112–2122 (2007).
26. Eggeling, C. *et al.* Direct observation of the nanoscale dynamics of membrane lipids in a living cell. *Nature* **457**, 1159–1162 (2009).
27. Jacobsen, V., Klotzsch, E. & Sandoghdar, V. Interferometric detection and tracking of nanoparticles. in *Nano Biophotonics* (eds., Masuhara, H., Kawata, S. & Tokunaga, F.) 143–160 (Elsevier, Amsterdam, 2007).
28. Damm, E.M. *et al.* Clathrin- and caveolin-1independent endocytosis: entry of Simian Virus 40 into cells devoid of caveolae. *J. Cell Biol.* **168**, 477–488 (2005).
29. Kusumi, A. *et al.* Paradigm shift of the plasma membrane concept from the two-dimensional continuum fluid to the partitioned fluid: High-speed single-molecule tracking of membrane molecules. *Annu. Rev. Biophys. Biomol. Struct.* **34**, 351–378 (2005).

ONLINE METHODS

Preparation of supported lipid bilayers. Supported lipid bilayers were formed by the vesicle drop method[30]. All lipids were dissolved either in $CHCl_3$:CH_3OH (4:1) or in pentane. Dioleoylphosphatidylcholine (Avantilipids) was doped with ganglioside GM1 (Avantilipids) at different concentrations (0, 0.05 and 1 mol%), dried to a film and kept under vacuum for at least 2 h. Bilayer buffer (BB; Millipore water, 150 mM NaCl, 2 mM $CaCl_2$ and 50 mM HEPES (pH 6.8); Sigma Aldrich) was added to a concentration of 0.5 mg ml^{-1} of total lipid and the lipid film was hydrated for at least 1 h. The turbid solution was sonicated for 20–30 s at full power in a tip sonicator on ice and centrifuged for 30 min at top speed in a tabletop centrifuge to remove debris and multilamellar vesicles. Standard cover glass was cleaned with piranha solution (H_2SO_4:30% H_2O_2, 3:1) and dried under N_2. The clean cover glass was mounted in a custom-made microscopy chamber and the vesicle solution was added at 100 μg ml^{-1} for 30 min for the formation of a single supported lipid bilayer on the cover glass. Excess vesicle solution was washed away with ten exchanges of 1 ml of fresh BB, and the fluidity and continuity of supported membrane bilayers were assured by FRAP experiments on fluorescein-DPPE incorporated in parallel samples as described previously[15]. Biotinylated SV40 virus-like particles (VLP) were added at 50 ng ml^{-1} for 15 min followed by 5 μl of a 1:10,000 dilution of streptavidin-coupled 655 nm QDs (Invitrogen; Qdot 655–streptavidin conjugate). In the absence of SV40, no binding of QDs to the supported lipid bilayer was observed. After 15 min, the supernatant was replaced with an excess volume of BB.

Virus-like particle (VLP) purification and labeling. SV40 VLPs were generated as described previously[31]. A lysate of SF9 cells containing expressed SV40 VP1 was a kind gift from A. Oppenheim. The lysate contains fully assembled SV40 VLPs as well as assembly intermediates and unassembled VP1 protein. To purify the fully assembled VLPs, the lysate was clarified by centrifugation for 30 min at 10,000*g* in an Eppendorf microfuge. The clarified supernatant (0.5 ml) was centrifuged at 4 °C for 2.5 h at 160,000*g* in a Beckmann SW41Ti rotor through a 5–20% (wt/vol) linear sucrose gradient with a 0.5 ml 60% (wt/vol) sucrose cushion in 10 mM HEPES, pH 7.4, containing 1 mM $CaCl_2$. After fractionation, 0.5 ml fractions were analyzed by transmission electron microscopy following negative staining, and fractions with homogeneous intact particle populations were pooled. The purified particles were dialyzed against bilayer buffer and stored at −80 °C. SV40 VLPs were labeled with biotin using a kit from Pierce. Biotin was covalently coupled to SV40 VLPs in 0.2 M $NaHCO_3$, pH 8.3 using a fivefold molar excess of biotin relative to VP1 protein for 2 h. Unbound biotin was removed by chromatography with a Nap-5 column (Amersham Biosciences) against BB and resulting fractions were checked by SDS-polyacrylamide gel electrophoresis and silver staining before being pooled.

Experimental setup. The experimental arrangement used to perform interferometric scattering detection (iSCAT) is shown schematically in **Figure 1c**. The output of a low-noise diode-pumped solid-state laser at a wavelength of 532 nm (World Star Tech) is magnified by a ×5 beam expander, passed through two acousto-optic deflectors (AOD; AA Opto Electronic), a telecentric lens imaging system and two beam splitters before entering a home-built inverted microscope. The deflection of the beam path caused by the AODs is imaged by the telecentric system, consisting of two 2-inch $f = 300$ mm focal length lenses, onto the back focal plane of the microscope objective to scan the focus across the sample. The incident light reflected at the glass-water interface and scattered by the sample as well as any fluorescence emission are collected by the same objective. Fluorescence emission centered around 655 nm from individual QDs is reflected by the dichroic beam splitter and stripped of the remaining excitation light by a 620 nm long-pass filter (Omega filters) before being imaged onto an electron-multiplying CCD (EMCCD, Andor iXon). We chose far red–emitting QDs to minimize the influence of background fluorescence excited by the incident laser. Scattered and reflected incident light passes the dichroic and is partially reflected at the second 50:50 beam splitter and directed toward a second CCD (Andor Luca S). Both beam splitters are thick (1 cm) 1-inch-diameter optics to prevent reflections from entering either the objective or reaching the CCD, which results in poor image quality. The telecentric lenses are placed at a slight angle (10°) for the same reason. Similarly, the iSCAT camera is tilted (10°) to minimize interference due to multiple reflections caused by the camera window.

Rapid beam scanning is achieved by driving each of the AOD controllers with separate function generators (Stanford Research Systems). Optimum iSCAT image quality was achieved using a triangle function at 40 and 39 kHz for the *x* and *y* channels, respectively. The phase of the latter was offset by 90° and they were given an amplitude of 0.6 and 0.4 V, respectively. This results in an illuminated region slightly larger than the area of the CCD chip. The function generator controlling AODx simultaneously provided a trigger output, which was used to synchronize both the second function generator and thereby AODy as well as the two CCD cameras. The number of cycles for each triangle function was adjusted to match the exposure time of the CCDs. This process was repeated after a delay required for the CCD to read out. Synchronization of the fluorescence and iSCAT channels was precise within 50 μs and verified by monitoring the trigger outputs of the cameras.

Achievement of nanometer spatial resolution. The incident beam diameter was optimized to avoid total internal reflection at the glass-water interface, which results in a complication of the observed iSCAT signal. For fluorescence detection, the magnification was adjusted to achieve optimum localization accuracy (108 nm $pixel^{-1}$). For iSCAT, however, it is necessary to detect as many photons as possible per unit area. To achieve a localization accuracy below 2 nm, SNRs >30 are necessary. Given that single SV40 VLPs produce about 3% contrast, the background induced fluctuations must not exceed 0.1%, which corresponds to 10^6 detected photoelectrons. Most CCD cameras, however, are unable to collect more than 20,000 electrons per pixel if saturation is to be avoided. This means that the electrons of at least 50 pixels have to be summed to achieve the necessary accuracy at maximum imaging speed. In practice, we used ×1,388 magnification to collect ~2 million electrons for an effective pixel size of 100 nm and thereby achieved ~2 nm localization accuracy with respect to the center of mass of the virus.

doi:10.1038/nmeth.1395

The incident laser power (1.5 mW at 25 Hz, 5 mW at 130 Hz) was demanded by the requirement of achieving sub-5 nm localization accuracy in the fluorescence channel by excitation of the QD. The average photon flux taking into account beam scanning over a 10 × 10 μm area amounts to 5 kW cm^{-2}. For an absorption cross-section of 10^{-15} cm^2 per QD, this results in 1.25×10^7 excitations per second. In light of the high numerical aperture (NA) and the 95% quantum efficiency of the EMCCD we can assume a detection efficiency greater than 10% even after taking into account losses owing to the objective, mirrors, filters and lenses. In the on state, unity fluorescence quantum yield of QDs would result in ~10,000 detected photons per image. The reported accuracy of ~4 nm, however, corresponds to ~4,000 detected photons. This lower value is likely due to fluorescence blinking during the exposure time. It is noteworthy that when using beam scanning at these high incident light intensities we observed relatively few completely dark periods as opposed to standard wide-field illumination.

Image analysis. Image sequences containing 1,000 images were acquired simultaneously on both fluorescence and iSCAT channels. The latter images show several features due to residual reflections and the surface roughness of the glass (**Supplementary Fig. 1a**). The only mobile portion of these images, however, originates from virions diffusing on the membrane. Simple 1:1 subtraction of an image lacking virions (**Supplementary Fig. 1b**) from each one in the series removed all spurious signals such that only features owing to diffusing viruses remain. The remaining images (**Supplementary Fig. 1c**) were purely shot noise–limited, given that camera noise is orders of magnitude smaller. The observed slow background fluctuations have recently been shown to disappear through the use of a window-free CCD camera. The precise center of mass position of the virus (x_{VCM} and y_{VCM}) and the QD (x_{QD} and y_{QD}) in each image as well as the accuracy of the measurement is determined by numerical fitting to a two-dimensional Gaussian function as discussed in detail previously[4]. Connecting the positions in subsequent images created trajectories of the absolute center of mass motion of the virus and QD. Images in which the fluorescence localization accuracy dropped below 10 nm were excluded from the trajectories.

Image registration. To observe not only the absolute motion of the QD and the virus but also correlate their relative motion, it was necessary to overlap their trajectories with nanometer precision. We adhered closely to a previously published procedure[19]. Briefly, a 100 nm uniformly doped fluorescent bead was moved in 100 nm steps throughout the field of view using a closed-loop piezo scanner with 1 nm accuracy. Acquisition of iSCAT and fluorescence images at each position and determining the center of mass of each by numerical fitting resulted in two correlated grids on the two cameras. The known step size was used to validate the magnification of the optical system and scale the two reference grids appropriately (**Supplementary Fig. 2a**). We used an algorithm that maps the iSCAT position onto the fluorescence channel by using the distance-weighted average shift from its four nearest neighbors in the reference grids. To check the performance of the registration procedure, we recorded additional iSCAT and fluorescence grids using other fluorescent beads and superimposed the two using the original reference grids. The average error was 3.4 nm (**Supplementary Fig. 2b**).

30. Kalb, E., Frey, S. & Tamm, L.K. Formation of supported planar bilayers by fusion of vesicles to supported phospholipid monolayers. *Biochim. Biophys. Acta* **1103**, 307–316 (1992).
31. Kosukegawa, A. *et al.* Purification and characterization of virus-like particles and pentamers by the expression of SV40 capsid proteins in insect cells. *Biochim. Biophys. Acta* **1290**, 37–45 (1996).